RESEARCH ARTICLE

Editor's Choice

ADVANCED
OPTICAL
MATERIALS

www.advopticalmat.de

Observing Metallic Carriers in Highly Faceted Plasmonic Cd$_2$SnO$_4$ Inverse Spinel Nanocrystals

Raul E. Ortega, Robert B. Smith, Jason E. Kuszynski, Aaron Bayles, Stephen A. McGill, Naomi J. Halas, Robert W. Schurko,* and Geoffrey F. Strouse*

Correlating data from optical, structural, and theoretical methods allows the properties of highly faceted Cd$_2$SnO$_4$ (CTO) inverted spinel plasmonic semiconductor nanocrystals (PSNCs) to be fully evaluated. The use of Sn(II) in the colloidal reaction for CTO results in reproducible octahedral PSNCs with an aspect ratio of 1.30. Correlating extinction spectra with magnetic circular dichroism yields a carrier density ($n = 5.19 \times 10^{19}$ cm^{-3}) and carrier effective mass ($m^* = 0.022 m_e$) respectively. ^{113}Cd and ^{119}Sn solid-state NMR experiments show clear evidence of metallic-like carriers in CTO NCs based upon the observation of Knight shifts. These data suggest that carrier formation in CTO arises from Sn antisite occupation of octahedral Cd sites (Sn$_{Cd}$). From a broader perspective, the results point to wide-bandgap spinels as being an important but understudied class of plasmonic PSNCs.

1. Introduction

Plasmonic nanomaterials are observed to enhance photocatalysis,[1] photovoltaics,[2] sensors,[3] telecommunications,[4] night vision,[5] and photothermal therapy.[6] While the mechanistic origins of these enhancements are still under discussion, developing new cost-effective plasmonic nanomaterials that have high carrier densities and tunable plasmon features is critical to the future implementation of these findings. Not surprisingly, the development of plasmonic semiconductor nanocrystals (PSNCs) using wide bandgap (E_g), metal oxide (MO$_x$) semiconductors is beginning to replace noble nanometals for plasmonics research, reflecting their lower cost, high carrier densities ($n > 10^{19}$ cm^{-3}), transparency in the visible spectral region, and the possession of a tunable localized surface plasmon resonance (LSPR) frequency.[7–11] MO$_x$ PSNCs are an important class of n-type plasmonic materials shown to exhibit high conductivity and mobility in thin films and form the basis of transparent conducting oxide industrial technology.[12–17] The LSPR frequencies of MO$_x$ PSNCs are predictable using dielectric modeling of the carrier effective mass (m^*), carrier density (n), band parabolicity, and degree of compensation centers arising from lattice defects.[8,18–24] The most heavily studied n-type MO$_x$s rely on oxygen vacancies (V$_O$) to induce carriers in the conduction band (CB); however, the presence of V$_O$'s is associated with rapid carrier trapping following LSPR excitation in PSNCs.[25] Recently, it has been theorized that antisite occupation in inverted spinels can lead to n-type doping in nonstoichiometric phases without the involvement of V$_O$.[26] Traditional spinels formed from A^{2+}/B^{3+} cations (A and B are transiton metals), are often employed as optical host materials,[27–29] while spinels formed from A^{2+}/B^{4+} are much less explored. Spinels are a chemically resistant ternary line phase that can form as a normal AB$_2$O$_4$, inverted A(AB)O$_4$, or a combination (A$_{1-x}$B$_x$)[A$_{x/2}$B$_{1-x/2}$]$_2$O$_4$ of the two phases. In the normal spinel, the A-cation occupies a tetrahedral (T_d) site while the B-cation occupies an octahedral (O_h) site. In the inverted spinel, the A-cation occupies both the T_d and O_h lattice sites, while the B-cation occupies only the O_h site. In inverted spinels, antisite occupation can occur, where one cation is located on a lattice site that would normally be occupied by the other cation. Increased carrier densities have been reported in thin films for these types of systems, suggesting antisite populations may play an effect.[30–32] Further study on inverted spinel MO$_x$ PSNCs and the nature of the carriers' parentage can open new frontiers for the discovery of semiconducting materials for applications in photonics and electronics.

The n-type Cd$_2$SnO$_4$ (CTO) and n, p-type Ga$_2$FeO$_4$ (GFO) NCs have been reported to exhibit absorption features tentatively assigned to plasmons by fitting the Drude model.[7,33] Density functional theory (DFT) calculations on CTO, GFO, and n, p-type FeAl$_2$O$_4$, support the hypothesis that CTO and GFO are able to support high carrier densities without V$_O$ formation.[34] CTO is an important wide (E_g) semiconductor, as its carrier properties do not depend on V$_O$, and it is very chemically stable. CTO is nonmagnetic with carrier densities on the order of 10^{19}–10^{20} cm^{-3}

R. E. Ortega, R. B. Smith, J. E. Kuszynski, R. W. Schurko, G. F. Strouse
Department of Chemistry and Biochemistry
102 Varsity Way Chemical Sciences Laboratory
Florida State University
Tallahassee, FL 32306, USA
E-mail: rschurko@fsu.edu; gstrouse@fsu.edu
R. B. Smith, S. A. McGill, R. W. Schurko
National High Magnetic Field Laboratory
Tallahassee, FL 32310, USA
A. Bayles, N. J. Halas
Department of Chemistry and Laboratory for Nanophotonics
Rice University
Houston, TX 77005, USA

**ADVANCED
SCIENCE NEWS**

www.advancedsciencenews.com

**ADVANCED
OPTICAL
MATERIALS**

www.advopticalmat.de

and carrier effective masses ranging from 0.33 to $0.028 m^*/m_e$, depending on synthetic conditions.[7,35–40] CTO has been of interest since the 1970s, following reports that thin film CTO is a potential transparent conducting oxide competitive with the well-known $Sn:In_2O_3$.[39–41] In thin film CTO, it was unclear whether the observed carriers were attributable to V_O, typically observed in n-type MO_xs, or antisite formation from the non-stoichiometric Sn to Cd ratio. Siegel later revealed that CTO crystallizes in the inverse spinel structure rather than the orthorhombic structure in thin films, leading to improved optoelectronic properties attributable to self-doping by the antisite population of the Cd O_h site (Sn_{Cd}).[42] In CTO, the population of Sn(IV) is greater than Cd(II) at the O_h site, deviating from the stoichiometric formula ($Cd_{2-x}Sn_{1+x}O_4$), and leading to carrier formation by introducing electrons into the CB from the Sn(IV) atoms. The role of antisite occupation in CTO was theoretically supported by Zhang et al.,[32] and charge carriers in CTO at the nanoscale were reported to generate a feature in experimental NIR spectra that were assigned as an LSPR.[7] The reported CTO thin film results suggest CTO PSNCs are a promising material for antisite carriers lacking V_O. A recent study suggests that CTO nanocrystals are plasmonic; however, direct evidence of the carrier's effective mass, electron versus hole doping, and metallic-like carriers expected for a PSNC have not yet been reported.

In this work, direct evidence of metallic character in highly faceted CTO PSNCs is provided by the observation of large Knight shifts in ^{113}Cd and ^{119}Sn solid-state NMR (SSNMR) spectra, which can be correlated with the appearance of an LSPR in the NIR. The 19 ± 2 nm CTO PSNCs are passivated by oleic acid and exhibit an octahedral motif consistent with the cubic crystal structure observed in powder X-ray diffraction (pXRD). The LSPR feature centered at 0.52 eV (2384 nm) is observed to be trimodal due to octahedral faceting of the CTO PSNCs (i.e., corner, edge, and face contributions to the LSPR). Using m^* determined from magnetic circular dichroism (MCD), the LSPR extinction can be fit to a three-mode simplified Drude approximation (SDA) to extract n. The LSPR and E_g are observed to shift to lower energy with the addition of nitrosonium tetrafluoroborate ($NOBF_4$), corresponding to free carriers being titrated from CTO. The observed bathochromic shift in LSPR is consistent with the Drude model,[43] while the E_g shift to lower energy is consistent with Burstein–Moss behavior.[44,45] The corroborating data provides direct evidence that the carrier population in CTO is antisite-driven, confirming the earlier speculation by Ye and coworkers.[7] From a broader perspective, this study of highly-faceted CTO PSNCs suggests that further research on inverted spinels may lead to the discovery of new nanomaterial spinels for plasmonic materials and applications.

In addition, the study establishes a powerful toolset to interrogate carrier behavior in PSNCs: when MCD and SSNMR measurements are deployed, the role of n-type dopants can be analyzed. There are relatively few reports of SSNMR spectroscopic characterization of PSNCs, despite its ability to measure both isotropic and anisotropic (i.e., orientation-dependent) NMR interactions, which provide insight into local atomic environments in their cores and on their surfaces, nanoparticle (NP) size, coordination chemistry, surface characteristics, and electronic structure.[46,47] Aside from the potential influences of isotropic

chemical shifts and chemical shift anisotropies (CSAs) that impact the SSNMR spectra of spin-1/2 metal nuclides like ^{113}Cd and ^{119}Sn in NPs, it is sometimes possible to observe Knight shifts (KS) and Knight shift anisotropies (KSAs),[48–50] which arise from the presence of conduction electrons in metallic NPs[51,52] or free carriers in semiconducting NPs.[53] KS and KSA typically manifest in SSNMR spectra as large frequency shifts (positive or negative) and extreme broadening, respectively, and are very often observed in the SSNMR spectra of conducting metals,[54,55] as well as other solid materials that conduct electricity (like semiconductors).[56] Of relevance to the current work is the measurement of Knight shifts from ultra-wideline SSNMR spectra (i.e., powder pattern breadths >250 kHz),[57,58] and their correlation to E_g structure and the locations of free carriers in the NPs.[59] SSNMR spectroscopy adds to the tools available to PSNC researchers for unraveling the properties of this important class of materials with a broad range of technologically relevant applicability.

2. Results and Discussion

2.1. Optical and Structural Analysis

In **Figure 1**, characterization data is provided for highly faceted octahedral CTO PSNCs achieved by adapting the method of Ye.[7] The highly faceted CTO is prepared through the use of Sn(II) acetate as the precursor instead of Sn(IV) acetate to encourage the formation of the inverted spinel by coupling the chemical reduction of Cd(II) → Cd(0) with concomitant oxidation of interstitial Sn(II) → Sn(IV). Evidence for nucleation and growth of CTO by formation of Cd metal but not CdO, Sn, SnO, or SnO_2 is evidenced by analysis of the isolated nanoparticles from the raw batch versus selective isolation of the Cd and the CTO by sequential centrifugation steps (Figure S1, Supporting Information). The Sn(IV) and Cd(II) oxidation states in the CTO sample, following Ar^+ beam sputtering to remove surface ligands, are confirmed by X-ray photoelectron spectroscopy (XPS) (Figure S2, Supporting Information). The reaction drives the efficient formation of the desired CTO inverted spinel line phase with higher reproducibility than the previously described route. The Cd to Sn ratio of the isolated CTO nanocrystals measured by energy dispersive X-ray spectroscopy (EDS) analysis is 1.0:1.2, leading to an average composition of $Cd_{1.86}Sn_{1.14}O_4$ (Table S1, Figures S3 and S4, Supporting Information). The isolated oleic acid-passivated colloid is emerald green in color (Figure S5, Supporting Information).

In Figure 1a, pXRD data is shown for the CTO PSNCs compared to the PDF 01-080-1468 card for cubic (CTO) inverse spinel, where * indicates the presence of trace SnO_2, <1.5% based on whole-powder-pattern fitting analysis (Figure S6, Supporting Information). In the pXRD pattern, the (111) reflection is clearly observed in the isolated CTO samples consistent with a high degree of crystallinity and/or a high degree of faceting on the isolated CTO PSNC samples. In Figure 1b, high-angle annular dark-field scanning transmission electron microscopy (HAADF-STEM) images of the ensemble of CTO PSNCs clearly show an octahedral topology, with an octahedral aspect ratio of 1.30 and dimensions of 18.9 nm (long) × 14.5 nm (short) (Figures S9 and S10). The

**ADVANCED
SCIENCE NEWS**

www.advancedsciencenews.com

**ADVANCED
OPTICAL
MATERIALS**

www.advopticalmat.de
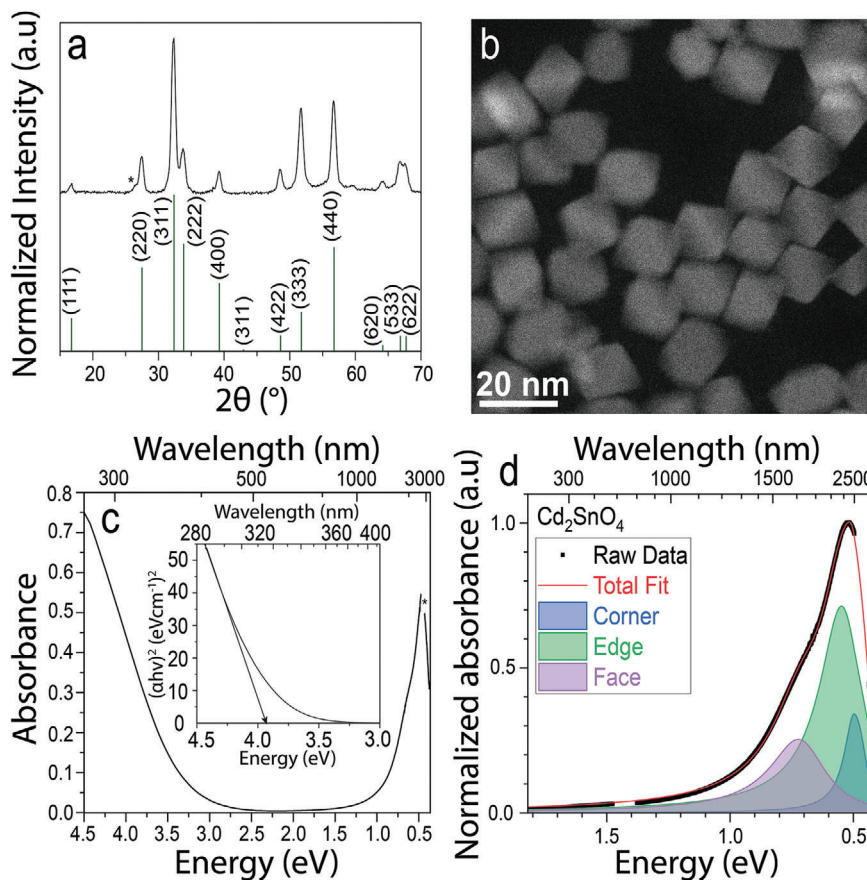
Figure 1. Optical and structural characterization of CTO nanocrystals. a) pXRD of CTO PSNCs with corresponding inverse spinel CTO reflections. b) HAADF-STEM of CTO PSNCs showing octahedron-like shape. c) UV–vis–NIR absorption spectrum with a Tauc plot inset showing a calculated optical E_g of 3.89 eV. d) Extinction spectrum of the LSPR fitted to a three-mode simplified Drude approximation illustrating the corner, edge, and face contributions.

long axis has an 8% length distribution with an 11% width distribution along the short axis.

The quality of the octahedra can be assessed by high HAADF-STEM images in Figure 1b and **Figure 2**. The isolated CTO PSNCs form as highly faceted 19 ± 2 nm octahedra, exhibiting truncated vertices along the z-direction. In Figure 2a, tilt-dependent images (+30°, 0°, −30°) confirm the truncated octahedral morphology assignment. In Figure 2b, two adjacent CTO PSNCs are observed demonstrating different morphology depending upon orientation. High resolution and tilt-dependent HAADF-STEM allows the lattice fringe patterns to be indexed to the (220) ($d_{(220)}$ = 3.24 Å), (222) ($d_{(222)}$ = 2.65 Å) and (111) ($d_{(111)}$ = 5.30 Å) planes. A facet angle of 109.5° is measured for the PSNC facet edges, consistent with the expected dihedral angle for octahedral morphology. The HAADF TEM can be directly compared to a 3D atom reconstruction (Figure 2c–f) for CTO imaged as top-down along the z-direction, (001) facet, and laying on a (111) facet for the octahedra tilted on their sides. The presentation of the large (111) facet in a controlled PSNC growth condition is expected, as the (111) facet in CTO is the lowest energy surface for the cubic spinel structure.[60] The implementation of Sn(II) as the reactant to control Cd reduction appears to regulate CTO growth rates, allowing well-faceted octahedral PSNCs to be isolated, which has not been previously reported.

In Figure 1c, the E_g absorption and LSPR extinction spectra are plotted. The intense emerald color of the CTO is assigned as arising from the SWIR (short wave infra-red) LSPR extinction. The observed absorption edge in the optical spectra at >3.0 eV (333 nm) is assigned to the onset of E_g, while the feature at 0.47 eV (2638 nm) is assigned to the LSPR. In Figure 1c inset, a Tauc plot is plotted to yield an E_g = 3.89 eV (319 nm), which is in good agreement with previously reported values for spherical CTO NCs (E_g = 3.81 eV)[7] and thin films (E_g = 3.60 eV).[61]

The LSPR exhibits three modes, with peaks at 0.73 eV (1698 nm), 0.55 eV (2264 nm), and 0.50 eV (2480 nm) that are attributed to face, edge, and corner contributions to the LSPR, respectively, as seen in Figure 1d.[20,62] The distinct modes are expected based on the octahedral shape observed by HAADF-STEM, leading to the separation of the LSPR into three different modes corresponding to the face, edge, and corner contributions. While the tip and face contributions of the LSPR are usually observed experimentally, the edge is typically observed only in theoretical models.[20,62,63] The face, edge, and corner contributions to the LSPR yield quality factors (Q-factor) of 3.00, 2.98, and 4.70 respectively, comparing well with reported values for Sn:In$_2$O$_3$ (ITO) and In:CdO.[64,65] The previously reported Q-factor for spherical CTO PSNCs is 1.92.[7] The volume corrected LSPR extinction scales with $n^{2/3}$.[66]
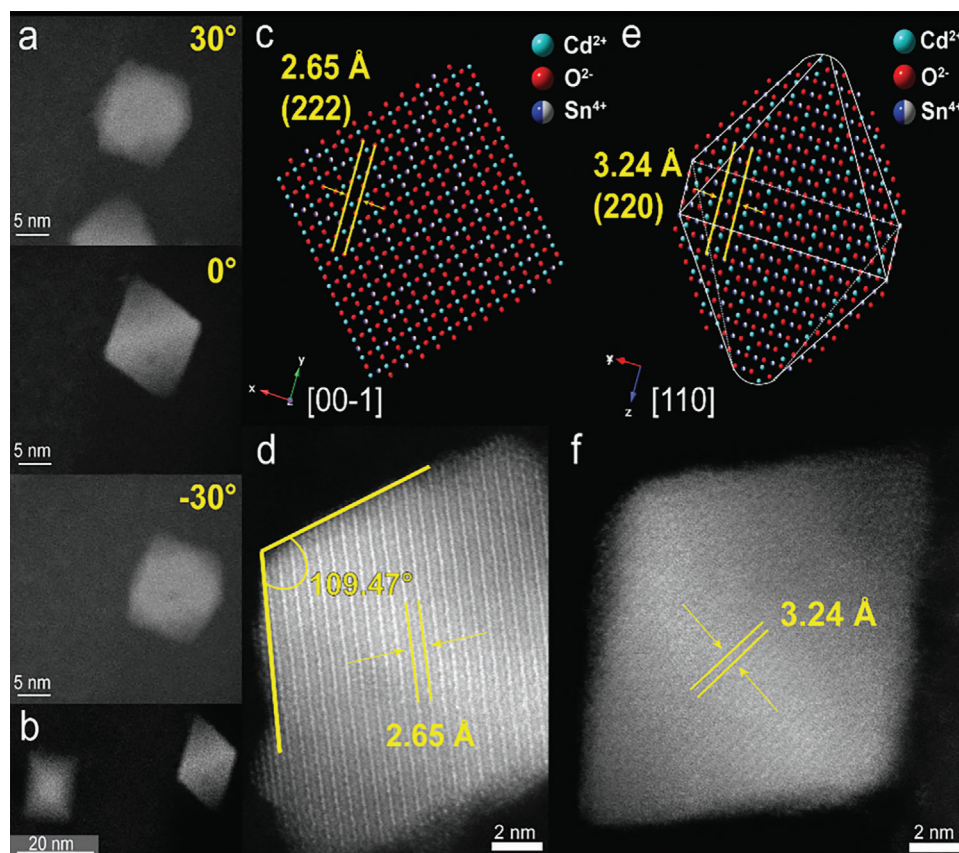
Figure 2. HAADF-STEM experiments of CTO PSNCs. a) Tilting images at 30°, 0°, and −30° probing different PSNC orientations showing octahedron-like shape. b) Two neighboring PSNCs express different morphologies depending on the PSNC orientation relative to the electron beam. c,d) Simulated and HAADF-STEM of CTO PSNCs showing d-spacing of 2.65 Å (222). An obtuse angle of 109.47° is drawn to illustrate the dihedral angle for an octahedron shape. e,f) Simulated and HAADF-STEM of CTO PSNCs showing d-spacing of 3.24 Å (220).

Following the procedure of Jain et al.,[67] the volume corrected extinction value for CTO is 9.67 µm⁻¹ (10^{19} carriers cm⁻³). For comparison, extinction values between 15 and 55 µm⁻¹ are reported in ITO for carrier densities of ≈10^{20} carriers cm⁻³, while $Cu_{2-x}Se$ (≈10^{21} carriers cm⁻³) has an extinction of 23.50 µm⁻¹.[64]

The assignment of the 0.5–0.73 eV feature to an LSPR is supported by a dielectric solvent shift study, with an extracted sensitivity of 5.29×10^6 nm² RIU⁻² (Figure S9, Supporting Information), which is the same order of magnitude observed in ITO PSNC's.[20] The observed sensitivity reflects changes in solvent refractive index, which correlates with PSNC depletion layer thickness and doping concentration.[68] The change in UV–vis–NIR LSPR and E_g features following chemical titration of a micromolar CTO trichloroethylene solution by the one-electron oxidant, $NOBF_4$, is shown in Figure S10 (Supporting Information). Fitting of the LSPR frequency shift as a function of $NOBF_4$ concentration to a linear function [linear portion < 3 µmol] provides confirmation of the LSPR assignment and an estimate for the concentration of $NOBF_4$ for total carrier titration by extrapolation. It is important to note that the use of strong oxidants does not allow accurate assessment of carrier density in a PSNC, since $NOBF_4$ is known to oxidize not only the introduced carriers but also surface states and compensation centers in PSNCs.[11,69]

The observed band edge shift with increasing occupation of Sn_{Cd} on the Cd_{Oh} site can be interpreted by inspection of density functional theory (DFT)-derived density of states (DOS) for CTO with varying Sn occupation (**Figure 3**). In the DOS, the valence band (VB) is comprised primarily of O $2p$ orbitals, while the CB is a mixture of Cd $5s$ and Sn $5s$ orbitals. As the concentration of Sn_{Oh} (Sn_{Cd}) in $(Cd_{1.00})_{Td}(Cd_{1.00-x}Sn_{1.00+x})_{Oh}$ increases from x = 0 to x = 1, both VB and CB energies decrease with respect to the Fermi level. It is also important to note that in the CB, the ratio of Cd to Sn $5s$ orbitals changes as expected as a function of Sn incorporation. For the pristine structure (Cd_2SnO_4), the Cd $5s$ contributions dominate the CB in comparison to the Sn $5s$ orbitals. When the Sn concentration increases to yield the $Cd_{1.5}Sn_{1.5}O_4$ structure, the Sn $5s$ orbitals become the main contributors to the CB DOS. As the concentration of Sn further increases leading to the formation of the $CdSn_2O_4$ structure, the CB is predominantly formed by Sn $5s$ orbitals, with a minimal contribution from Cd $5s$ orbitals. Inspection of Figure 3d illustrates the calculated optical E_g for the experimental stoichiometry $(Cd_{1.00})_{Td}(Cd_{0.86}Sn_{1.14})_{Oh}$ with a value of 3.84 eV in good agreement with the experimentally obtained optical E_g of 3.89 eV from Tauc plot analysis in Figure 1c.

ADVANCED
SCIENCE NEWS

www.advancedsciencenews.com

ADVANCED
OPTICAL
MATERIALS

www.advopticalmat.de
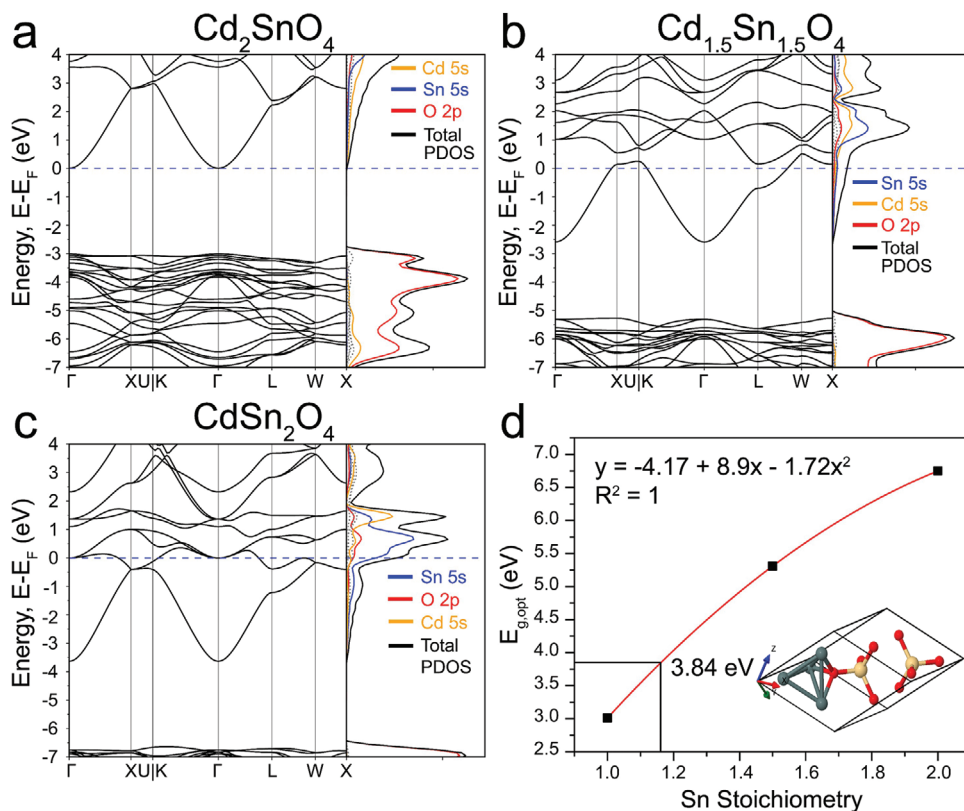
Figure 3. Overall density of state (DOS) and detailed orbital makeup of a) Cd_2SnO_4, b) $Cd_{1.5}Sn_{1.5}O_4$, c) $CdSn_2O_4$. d) Quadratic fit of the optical bandgaps calculated from the DOS as a function of Sn stoichiometry with an inset showing the representative unit cell for $Cd_{2-x}Sn_{x+1}O_4$ used for calculations. The fit yields an optical bandgap of 3.84 eV for an NC with a $Cd_{1.86}Sn_{1.14}O_4$ composition.

2.2. Evaluating m^* and n

While n can be estimated from the Drude model fits, this requires m^* to be known. The value of n is evaluated by fitting the observed plasma frequency (ω_p) to the Drude model, such that $\omega_p \propto \sqrt{(n/m^*)}$. The Drude model requires m^* to be assumed constant with size and defect densities, which has implicit bias, or is experimentally measured. Assuming A-term behavior, MCD can be used to extract m^* from the Zeeman splitting energy (E_z) of the LSPR extinction due to the cyclotron resonance phenomenon (Equations 1 and 2).[70–72] Combining the selection rules of left- and right-circularly polarized (LCP, RCP) light with a rigid-shift approximation, the cyclotron resonance effect experienced by free carriers is used to extract E_z and m^* for LSPR free carriers,

$$E_z = \omega_B^{RCP} - \omega_B^{LCP} \tag{1}$$

$$\omega_B^{LCP/RCP} = \omega_0 \pm \frac{qB}{2m^*} \tag{2}$$

where ω_B is the field-dependent plasma frequency, ω_0 is the field-independent plasma frequency, q is the elementary charge, B is the applied magnetic field, and m^* is the effective mass of an electron. The charge carrier ($e-$ vs $h+$) is determined from the effective charge (q) observed in the signage of the ΔA spectrum (MCD intensity). While measuring the LSPR is more accurate,

Radovanovic and coworkers showed that E_z, and subsequently m^*, can be evaluated by performing MCD on the E_g band edge, reflecting that a Burstein–Moss shift of the band edge (ΔEBM) occurs due to Fermi level changes directly associated with LSPR free carriers ($\Delta E^{BM} = (E_g^{CTO} - E_g^0) \propto \frac{n^{2/3}}{m^*}$).[73] In Equations (3) and (4), the n-dependent band edge shift can be related to the value of m^* by considering the magnetic field-dependent shift in the bandgap E_g^{LCP} versus E_g^{RCP} absorption or E_z. For the n-type semiconductor, only E_g RCP is observed (as has been previously reported) and is consistent with delocalized free electrons expected from LSPRs,[74]

$$E_z = E_g^{CTO\,LCP/RCP} = E_g^{CTO} \pm \frac{qB}{2m^*} \tag{3}$$

$$m^* = \frac{qBc}{2\pi(E_z)m_e} \tag{4}$$

thus, the field-dependent shift relative to the linear absorption E_g value (σ) allows E_z to be estimated ($E_z = 2\sigma$). Using the rigid-shift approximation, experimental linear absorption and MCD spectra are combined to extract E_z and calculate m^* using Equation (4).

In **Figure 4**, variable field (VH)-MCD spectra measured at 40 K from +6 to –6 T are shown for drop-cast CTO PSNC samples deposited from tetrachloroethylene (TCE) onto a quartz substrate. The MCD ΔA spectra are plotted as LCP minus RCP for both

**ADVANCED
SCIENCE NEWS**

www.advancedsciencenews.com

**ADVANCED
OPTICAL
MATERIALS**

www.advopticalmat.de
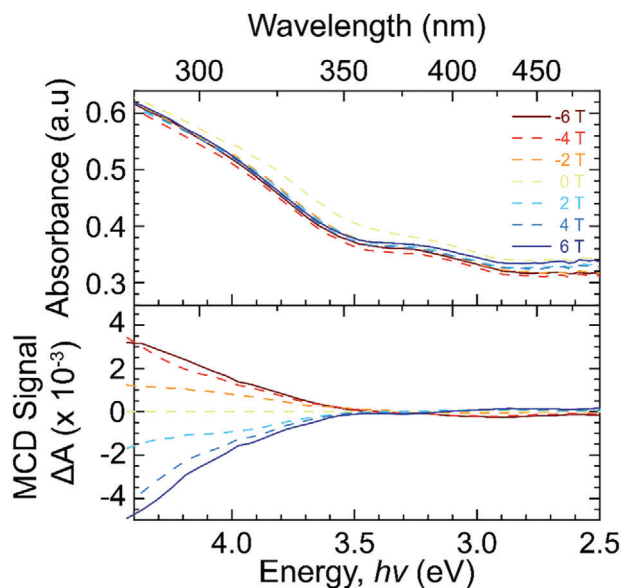
Figure 4. Dropcasted CTO on a quartz substrate was measured through magnetic field-dependent extinction (top) and VH-MCD spectroscopy (bottom) of the E_g band edge respectively.

0 T to 6 T and 0 T to –6 T. The collection of data at ± 6 T allows background rejection and improves signal-to-noise, reflecting the inversion of ΔA. In the linear absorption spectra for the drop cast sample, two absorption features in the E_g region are identifiable: a UV continuum region beginning at 3.50 eV assigned to the E_g edge, and a broad, weak feature at 3.22 eV. Only the E_g edge is observable in the solution for the sample, as previously reported.[7] The broad, weak absorption feature at 3.22 eV observed in the thin film has been previously reported but not assigned in literature for CTO thin films[75,76] and other n-type inverse spinel structures such as Zn_2SnO_4.[77] The origin of this feature likely arises from either a V_O population leading to a donor state near the band edge or a surface-bound Sn(II) complex to Sn(IV) charge transfer, as Sn(II) is observed as part of the surface passivating layer by XPS (Figure S2, Supporting Information). Further studies are underway to assign the feature that is only observable in the thin film configuration.

In Figure 4, negligible magnetic field dependence for the linear absorption spectra is observed. Using the linear absorption and MCD data from Figure 4 and Equation (4), m^* is calculated to be 0.022 ± 0.004 consistent with a report on doped CTO thin films.[35] In Equations (5) and (6), an alternative approach to extract m^* suggested by Gamelin and coworkers uses the Gaussian width and height of the linear absorption band edge (σ and A_0) and the MCD intensity ($\Delta A'$).[78] E_z is extracted from the MCD spectra, where $\Delta A'$ is obtained at an energy $E = (E_0 + \frac{\sigma}{\sqrt{2}})$ eV away from the Gaussian center (E_0).

$$E_Z = \frac{\sqrt{2e}}{2} \sigma \frac{\Delta A'}{A_0} \qquad (5)$$

$$f(E) = A_0 \exp\left(-\left(\frac{(E-E_0)}{\sigma}\right)^2\right) + y_0 \qquad (6)$$

The value of E_z approximated by comparing MCD signal intensity to linear absorption peak properties obtained from a simple Gaussian fit yields an m^* of 0.020 ± 0.005, which is within statistical agreement with results obtained from the first method. The extracted values of m^* are comparable to those obtained by electron energy loss spectroscopy (EELS for n-type CTO thin films, where m^* was calculated to be 0.02765 at the bottom of the CB.[35] While the results in this work show lower m^* than previously thin film results, it is not unreasonable due to the high crystallinity, symmetry perturbation, removal of observable V_O, and well-shaped PSNC morphology.[79]

The evaluation of m^* allows a value of n to be calculated from the Drude model by fitting the extinction spectra with $0.022m^*/m_e$ using a three-mode simplified Drude model to account for the octahedral shape (Figure 1d). The three-mode SDA model provides an average $n = 5.19 \times 10^{19}$ carriers cm^{-3}. For completeness, comparisons were made for the three-mode simplified Drude approximation (3-SDA); single-mode SDA (1-SDA); and the simplified, extended Drude approximation (SXDA), which takes into consideration the LSPR dampening terms. The fits are in good agreement with the average carrier density calculated through the three-mode model with the single mode SDA having a value of 3.56×10^{19} carriers cm^{-3}, and the SXDA has a value of 3.55×10^{19} carriers cm^{-3}. The fitting parameters are available in the supporting information (Table S2, Supporting Information).[80] As a final note, consistent with earlier reports in MO_x PSNCs, chemical titration of CTO with $NOBF_4$ is non-linear, yielding an overestimated n of 1.68×10^{22} carriers cm^{-3} (Figure S10, Supporting Information). The titration experiment in this work supports the earlier conclusion by Milliron and coworkers that chemical titration can yield unrealistic values for n due to untargeted oxidative damage.[11,69]

2.3. SSNMR Analysis of Charge Carriers

SSNMR spectroscopy provides resolution of atomic sites within a semiconductor nanocrystal,[81] where the observed frequency shift of the nucleus is dependent upon the site's coordination number, bonding (e.g., crystal field), and oxidation state. In the case of diamagnetic samples, this is reported as the chemical shift (CS). It is anticipated that, as carrier densities increase in PSNCs, charge carriers will become metallic-like above the Mott threshold.[82,83] The onset of metallic-like character can generate observable Knight shifts (KS) in SSNMR spectra.[59] The KS is a shift of the resonant frequency that occurs because of a local magnetic field induced at the nucleus due to the presence of conduction electrons. The magnitude of the KS is determined by several factors, including the DOS at the Fermi level, the local electron density, the nucleus, and the hyperfine coupling constant.[84] An increased number of electrons in the CB s orbitals tend to increase KSs since they have an increased probability of being located near the nucleus (increasing hyperfine interactions) as well as increasing the DOS due to CB broadening and Fermi-level contributions. Evidence for metallic behavior can be extracted from SSNMR measurements since KS $\propto \chi_s$, where χ_s is the electron spin susceptibility ($\chi_s \propto n^{1/3}$).[85]

Previous studies on PSNCs have reported small KSs in SSNMR spectra that are correlated to carrier densities. For instance,

**ADVANCED
SCIENCE NEWS**

www.advancedsciencenews.com

**ADVANCED
OPTICAL
MATERIALS**

www.advopticalmat.de
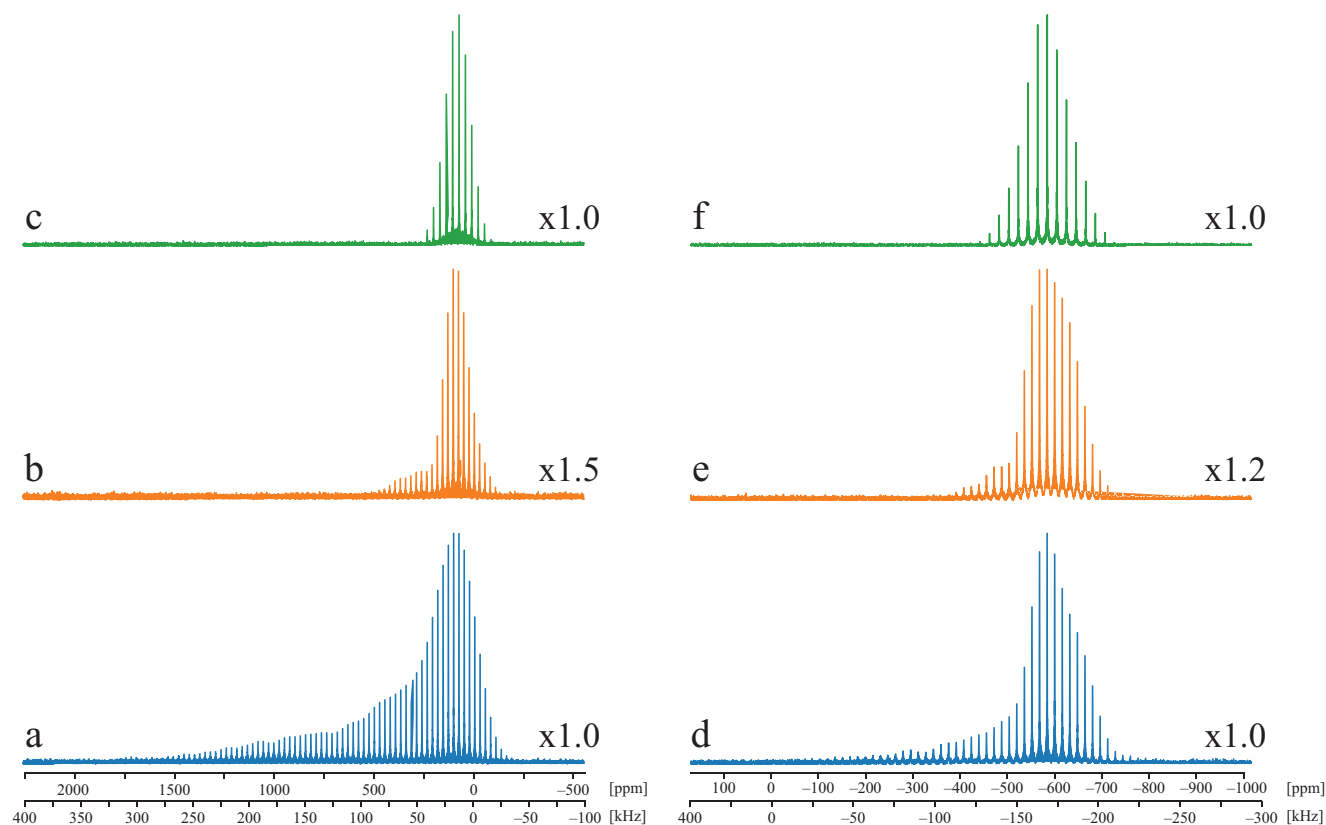
Figure 5. ^{113}Cd and ^{119}Sn SSNMR spectra of pristine a,d) and titrated b,e) CTO nanocrystals collected using a WURST-CPMG pulse sequence. ^{113}Cd and ^{119}Sn SSNMR spectra of pristine CTO samples c,f) were acquired using a CP-CPMG pulse sequence. All data were acquired at 18.8 T under static conditions.

Millstone and coworkers reported a KS and observation of the Korringa relationship for plasmonic $Cu_{2-x}Se$ PSNCs.[86] Additionally, Milliron and coworkers also described a KS for $F:In_2O_3$ PSNCs,[87] and the Strouse group reported a slight NMR frequency shift in ITO PSNCs.[21] A ^{113}Cd SSNMR study of bulk samples of CTO by MacKenzie and coworkers led to speculations that ^{113}Cd spectra had contributions from both KS and CS due to free electrons in the CTO samples.[88] It was suggested that the CS in the different CTO samples is proportional to the conductivity, yet no correlation was observed between this and the apparent KSs.[88] Finally, direct observations of KSs have been reported for noble metal nanoparticles and bulk narrow gap ($E_g <$ 2.5 eV) semiconductors.[89–92] Hence, the presence of a KS in the SSNMR spectra of PSNCs can provide evidence of the presence of free carriers; however, several factors are necessary for such observations, including a high n, low m^*, minimal magnetic susceptibility, and the presence of NMR-active isotopes.

In the cases of the CTO PSNCs, ^{113}Cd (S = ½) and ^{119}Sn (S = ½) SSNMR experiments can be used to measure potential KSs, especially since the CB of CTO is composed of both Cd and Sn 5s orbitals, where plasmonic-free electrons are expected to reside (Figure 3). In **Figure 5**, ^{113}Cd and ^{119}Sn SSNMR spectra are shown for pristine CTO (i.e., not titrated) and titrated CTO PSNC samples. The former has conduction electrons and the latter contains only a minimal or negligible number of carriers, as evidenced by the disappearance of the green color of the CTO powder after

titration (Figure S10, Supporting Information). Upon removal of free carriers by the addition of NOBF$_4$, the LSPR is lost and E_g shifts to lower energy, which is consistent with carrier removal (Figure S10, Supporting Information). In addition, no difference in the pXRD patterns is observed for the pristine and titrated samples (Figure S11, Supporting Information).

Comparison of the ^{113}Cd WURST-CPMG NMR spectra of stationary samples of the pristine (Figure 5a) and titrated (Figure 5b) CTO PSNCs exhibit distinct breadths of 345 kHz (1940 ppm) and 115 kHz (640 ppm), respectively. Though the patterns share similar features on their low-frequency ends, the larger breadth of the former is thought to arise from the distribution of KSs. Below, the rationale for this observation is explained by first considering the ^{113}Cd NMR spectra of the titrated samples (which in principle should have no conduction electrons), followed by those of the pristine sample.

The centers of gravity of the high- and low-intensity patterns for the titrated sample are at δ_{CG} = 150 and δ_{CG} = 225 ppm, respectively (Figure 5b). The distribution of chemical shifts arises due to the small size of the NCs, with Cd sites in their cores possessing shifts most resembling those of bulk Cd_2SnO_4, and those near the surface having greater variation due to an increased number of defects and potential interactions with surface ligands.[81,93,94] At first sight, it is tempting to assign these two powder patterns to Cd sites with six-coordinate ($Cd(O_h)$) and four-coordinate ($Cd(T_d)$) environments, since these are known

ADVANCED
SCIENCE NEWS

www.advancedsciencenews.com

ADVANCED
OPTICAL
MATERIALS

www.advopticalmat.de

to have values of δ_{iso} ranging from 150 to −100 ppm[95] and from 80 to 800 ppm, respectively.[81,96] However, if this was the case, both patterns would be visible in the corresponding ^{1}H-^{113}Cd CP-CPMG spectrum; in fact, only the pattern with $\delta_{CG} = 150$ ppm is observed. This suggests that i) the ^{113}Cd NMR patterns for the two sites in CTO may overlap in the static spectrum and ii) the pattern with $\delta_{CG} = 225$ ppm has some other origin.

This first point is addressed via examination of ^{1}H-^{113}Cd CP/MAS NMR spectra acquired with contact times of 3 and 8 ms (Figure S12, Supporting Information). Two broad peaks at $\delta_{iso} = 86$ and 46 ppm are clearly visible in each spectrum, with intensities that do not substantially change with different contact times. This suggests that these peaks do not arise from distinct chemical shifts of core and surface Cd species, since very different peak intensities would be observed for different contact times. One possibility is the tentative assignment of these peaks to the Cd(T_d) and Cd(O_h) sites, respectively (though quantum chemical calculations will likely be necessary to confirm this assignment). This assignment is provisional, since if Cd(T_d) sites are present, it is possible that they may have very long T_1 and/or very short T_2 relaxation time constants that prohibit their observation, which would require experiments of great lengths. It is also noted that high-frequency peaks arising from KSs are not observed in these CP/MAS spectra; this is in part due to the extraordinarily low S/N that is often observed in MAS NMR spectra of ultra-wideline NMR patterns, and in part due to the inefficiency of CP transfer to the core of the PSNCs (18.9 nm by 14.5 nm dimensions) where the Cd sites impacted by KSs likely exist (vide infra).

The second point is addressed by first considering the attribution of the broadening in the ^{113}Cd NMR spectra of the pristine samples to KSs, as well as the magnitude and field dependence of the KS. The powder pattern in the static ^{113}Cd NMR spectrum of the pristine sample (Figure 5a) has a total breadth of ≈345 kHz (1940 ppm), with its highest detectable shift at ≈1740 ppm. The high-frequency shift is far beyond the reported chemical shifts for non-metallic Cd compounds.[97] Furthermore, since the four- and six-coordinate Cd sites are extremely unlikely to lead to cadmium chemical shift anisotropies in excess of 300–400 ppm,[97] the broadening is attributed to a distribution of KSs. The maximum KS value is estimated by referencing the ^{113}Cd secondary standard Cd(NO$_3$)$_2$·4H$_2$O, $\nu_0(^{113}$Cd$) = 177.632$ MHz, which corresponds to $\delta_{iso} = -102$ ppm with respect to the primary standard of 0.1 M Cd(ClO$_4$)$_2$ at $\delta_{iso} = 0$ ppm).[95] From this, a maximum Knight shifted frequency of $K_{iso} = 0.309$ MHz (1740 ppm) yields the percent Knight shift as $\Delta K = K_{iso}/\nu_0(^{113}Cd) \cdot 100\% = 0.174\%$. This value is about 11 times the magnitude of that reported from ^{113}Cd SSNMR spectra of CdO ($\Delta K = 0.016\%$).[98] Additional confirmation of the observation of a distribution of KSs is provided by comparison of ^{113}Cd WURST-CPMG NMR spectra acquired at 14.1 and 18.8 T (Figure S13, Supporting Information) since the magnitude of the KS is proportional to the magnetic field strength. The broadening attributed to KSs is more pronounced in the 18.8 T spectrum (spectra on the kHz scale have distinct breadths, whereas those on the ppm scale are identical), where the ratio of the maximum KSs is $K_{iso}(18.8T)/K_{iso}(14.1T) = 306$ kHz$/230$ kHz $= 1.33$, matching the ratio of the higher and lower field strengths.

The contributions of atomic- and nano-level structures to the observed distribution of KSs are now considered. The range of the KSs is attributed to a distribution of distinct Cd environments, which vary in their nature from the core to the surface, by analogy to chemical shift distributions, vide supra. The dependence of the magnitudes of KSs in relation to the size and shape of NPs, locations of atoms within the NPs, and surface-ligand interactions are well known, especially for NPs comprised of conducting metals like Pt, Cu, and Ag,[47,52,99] allowing us to draw several tentative conclusions. The highest-frequency, Knight-shifted region of the pattern corresponds to nuclei of atoms in the core/interior of the PSNCs, since these are likely to have the most Cd 5s conduction electrons (due to a reduced number of defects). By contrast, Cd sites near the surface, which are in the depletion region of the CTO, have reduced or negligible KSs due to the presence of vacancies, defects, interactions with ligands/solvents, and surface reconstruction arising from Cd-ligand passivation.[100] This is confirmed by ^{1}H-^{113}Cd CP/CPMG spectra (Figure 5c), where the ^{113}Cd signal arises solely from ^{1}H spin polarization transferred from the oleic acid ligands on the surface of the PSNCs, yielding a spectrum resembling that of the titrated sample (cf. Figure 5b). Hence, returning to the second point above, the absence of extreme broadening in the ^{113}Cd NMR spectrum of the titrated sample, along with the presence of a small "tailing" to high frequency, likely indicates a small distribution of KSs, perhaps arising from residual conduction electrons after titration.

The corresponding set of ^{119}Sn SSNMR spectra for the pristine and titrated CTO samples (Figure 5d,e) reveal pattern breadths of 215 kHz (720 ppm) and 107 kHz (360 ppm), respectively. Analogous to the ^{113}Cd spectra, the narrow, low-frequency portions of the ^{119}Sn patterns exhibit chemical shift distributions, with values of $\delta_{CG} = -580$ ppm (from the titrated sample), corresponding to a single Sn(O_h) site.[101] Broadening in the ^{119}Sn WURST-CPMG spectra attributable to a KS distribution is prevalent for the pristine samples (again, tin CSAs for six-coordinate sites are not expected to produce the degree of observed broadening.)[97] However, the degree of broadening is less than that in the corresponding ^{113}Cd pattern (cf. Figure 5a,d). In the case of the pristine CTO PSNC sample (Figure 5d), the observable signal with the highest Knight shift is at ≈ −110 ppm. If $\nu_0(^{119}$Sn$) = 298.471$ MHz corresponds to the secondary chemical shift reference of $\delta_{iso} = 121$ ppm of solid SnO (with respect to the primary reference of SnMe$_4$ at $\delta_{iso} = 0$ ppm), the maximum Knight shifted frequency of $K_{iso} = 32\,832$ Hz (110 ppm), gives $\Delta K = 0.011\%$ (significantly smaller than the ΔK observed in the corresponding ^{113}Cd NMR spectra). Finally, the ^{1}H-^{119}Sn CP-CPMG SSNMR spectrum (Figure 5f) reveals that the low-frequency end of the pattern largely corresponds to surface cites, in line with the analogous ^{113}Cd data (cf. Figure 5e), confirming that KS signals arise from ^{119}Sn nuclei in the cores of the PSNCs. It is noted that the ^{119}Sn NMR spectra reveal no evidence of Sn(T_d) sites (the $\delta_{iso} = -200$ ppm for SnO, Figure 5d), which confirms the absence of Sn^{2+} oxide sites in the sample.[102]

A comparison of the KSs from the ^{113}Cd and ^{119}Sn SSNMR data infers of a higher number of free carriers in the CB from the Cd 5s orbitals than from those of the Sn 5s orbitals, especially given that the ratio of the ^{119}Sn and ^{113}Cd gyromagnetic ratios is $\gamma(^{119}$Sn$)/\gamma(^{113}$Cd$) \approx 1.7$, which would imply larger frequency

**ADVANCED
SCIENCE NEWS**

www.advancedsciencenews.com

**ADVANCED
OPTICAL
MATERIALS**

www.advopticalmat.de

shifts for ^{119}Sn if the contributions were equivalent. The development of a quantitative relationship between the ΔK values and carrier densities is challenging and beyond the scope of the current work, since it is possible that there are nuclei experiencing even higher KSs, which also may result in rapid T_2 relaxation that would render them unobservable in CPMG-type experiments – though this could be addressed with variable-temperature measurements of KSs and T_1 values.

3. Conclusion

In this work, direct evidence for metallic-like carriers in highly-faceted, octahedral-shaped CTO PSNCs are grown by high-temperature colloidal methods using a Sn(II) source. The use of Sn(II), which has not been previously reported for CTO, appears to control growth and nucleation in CTO, allowing reproducible isolation of highly faceted PSNCs with low densities of V_O defects. The octahedral-shaped CTO exhibiting (111) faceting has a 1.30 aspect ratio. The morphology of the PSNC leads to a three-mode LSPR assignable to face, edge, and corner contributions of the dielectric function. The observation of a correlating band edge shift, attributed to carrier-induced Burstein-Moss behavior, corroborates the presence of free electrons in the CTO PSNC. Fitting the MCD for m^* allows the LSPR spectra to be fit to the Drude approximation. A value of n of $\approx 10^{19}$ cm^{-3} with an m^* of $0.022m^*/m_e$ is extracted from the spectral data. The low m^* can be interpreted as electrons in the CB possessing higher mobility due to the absence of donor–acceptor states arising from noncarrier-contributing defects in the PSNC sample. The value of m^* is consistent with reports for CTO in thin films prepared by chemical vapor deposition.

The low m^* value suggests metallic-like behavior for the n-type carriers in CTO, likely reflecting the low trap densities in the inverted spinel. The metallic character is confirmed by the observation of large Knight shifts for ^{113}Cd and ^{119}Sn SSNMR spectra. The differences in KS in the ^{113}Cd and ^{119}Sn spectra indicate that more free carriers originate from the Cd 5s orbitals than the Sn 5s, which is consistent with DOS CB calculations. The distributions of chemical shifts and Knight shifts in the ^{113}Cd and ^{119}Sn spectra of pristine and titrated samples suggest that the free carriers reside in the core of the PSNCs; this is reinforced by ^{1}H-^{113}Cd and ^{1}H-^{119}Sn CP/CPMG experiments, which yield signals corresponding only to Cd and Sn sites near or on the surface, none of which exhibit Knight shifts. The NMR results indicate surface ligation and the presence of a surface depletion region may result in carrier damping.

While CTO PSNCs are not new, the manuscript illustrates the importance of fully characterizing PSNCs to elucidate the carrier behavior in colloidally prepared plasmonic materials. The correlation of optical, structural, and computational methods suggests low V_O defect densities in the inverted spinel CTO grown by colloidal methods can lead to highly mobile free electrons. DFT calculations of DOS support the experimental results and illustrate that in CTO, Sn_{Cd} is the major contributor to carrier generation. The combination of MCD and UV–Vis–NIR allows extraction of PSNC parameters without requiring the assumption of the value of m^*, with MCD also providing clear evidence of plasmonic and n-type behavior.

The NMR-resolved KS measurements represent some of the first examples of KS being observed in wide-band PSNCs. SS-NMR provides a powerful tool for structural and electronic analysis of these materials that further support the presence of metallic-like electrons in the CTO system. Further studies are underway to elucidate size, aspect ratio, and antisite population effects, especially within the quantum-confined regime where surface states may impact carrier mobility due to increased scattering contributions.

4. Experimental Section

Powder X-Ray Diffraction (pXRD): pXRD patterns were collected with a Rigaku MiniFlex powder X-ray diffractometer using a Cu Kα source. The pXRD patterns were collected using a zero-background micro-powder plate. Scans were collected from 15 to 70° at a rate of 7° min^{-1} and a 0.05 step size.

Synthesis of Cd_2SnO_4 Inverse Spinel PSNCs: The CTO PSNCs were synthesized following a modified method from the one reported by Ye and coworkers,[7] where the original Sn(IV) source is substituted for a Sn(II) acetate precursor. In a three-neck round bottom flask fitted with a condenser and a thermocouple, cadmium acetylacetonate (Cd(acac)$_2$, 1.2 mmol) and tin(II) acetate (Sn(OAc)$_2$, 0.3 mmol) are combined with OA (7.5 mmol) and ODE (25 mL). The solution was degassed at 120 °C for 1 h, and then rapidly heated to 319 °C where was kept refluxing for 100 min until the solution turned dark black/grey indicating the nucleation of CTO PSNCs. The PSNCs were isolated by the addition of IPA, followed by selective precipitation of the smaller CTO in toluene from bigger metallic Cd particles that form as a byproduct. The isolated CTO PSNCs are then passed through a toluene gel permeation chromatography (GPC) column to remove excess ligands following the published procedure.[103] The PSNCs are kept in toluene or TCE for storage.

UV–Vis–NIR Spectroscopy: Purified CTO was dissolved in TCE for all optical measurements. The optical data were collected in a PerkinElmer Lambda 950 spectrometer. A 1 mm path length NIR quartz cuvette was used for all absorbance measurements. Spectra were corrected using TCE.

Transmission Electron Microscopy: HAADF-STEM and EDX measurements were performed at 300 kV on an FEI Titan Themis3 (scanning) transmission electron microscope.

Computational Details and Modelling of CTO PSNCs: Modeling of CTO octahedrons NCs was generated using the NanoCrystal software tool.[104] DFT + U calculations were performed using a plane augmented wave pseudopotential for O atoms and ultrasoft pseudopotentials for Cd and Sn atoms selected from the SSSP database[105,106] via QuantumESPRESSO.[107] The unit cells used for calculations were prepared by taking an initial bulk unit cell of CTO ($Fd\bar{3}m$, a = 9.174 Å, ICSD-69299),[108] symmetry reducing using SeeK-path,[109] and then atomically relaxing, resulting in three representative unit cells of $Cd_{4-x}Sn_{2+x}O_8$ (x = 0, 1, 2) to simulate increasing $[Sn_{Cd}]$ behavior on the electronic band structure. The resulting lattice parameters were kept constant for all unit cells, where a cubic structure ($Fd\bar{3}m$, a = 4.587 Å) was used, matching half the lattice parameter of ICSD-69299. The kinetic energy cutoff for charge density and wavefunctions were 600 and 75 eV respectively, while a Monkhorst k-point mesh of 4 × 4 × 4 was used to perform even sampling across the dielectric field of the Brillouin zone.[110] A nonself-consistent field calculation of 12 × 12 × 12 was used to obtain the projected density of states (DOS) and band diagrams. Hubbard U parameters were applied to Cd 4d (10 eV), Sn 4d (9 eV), and O 2p (8 eV) orbitals to better approximate the experimental E_g for CTO, as performed previously in the literature.[111]

NOBF4 Titrations: The one-electron oxidant (NOBF$_4$) was used in a similar manner to Conti et al.[21] A known concentration of purified CTO crystals was flushed under N$_2$ and brought into an inert atmosphere glovebox. A known concentration of the NOBF$_4$ in MeCN was slowly titrated into the CTO solution, shaken, and then left to react for 30 min. The sample was then transferred to a 1 mm quartz cuvette transparent in the NIR region and loaded into the PerkinElmer Lamba 950.

MCD Sample Preparation: Thin films of CTO PSNCs were prepared by drop-casting from a colloidal solution with TCE onto a quartz substrate. The concentration was mediated by monitoring the CTO E_g absorption using a Cary 50 Bio UV–vis spectrophotometer until absorption units of no more than 0.5 were obtained. Afterward, VGE-7031 varnish was applied to adhere the quartz substrate onto the optical probe for use in the cryostat.

Variable Field (± 6 T at 40 K) Magnetic Circular Dichroism (VH-MCD): VH-MCD was performed on a home-built system and was more thoroughly described in a previous report.[24] Deviations and critical components were described herein. After sample adhesion, the drop cast CTO was dried under vacuum prior to insertion into an Oxford Instruments HelioxTL Superconducting Spectromag. A Newport Xe Arc Lamp was used as the light source in combination with a ThorLabs Glan-Taylor linear polarizer (GLB-10) to linearly polarize incident light, followed by the use of a HINDS Instruments photoelastic modulator (PEM-100) for subsequent circular polarization. A Hamamatsu PMT amplified with a Femto current amplifier (LCA-200K-20 M) is used to measure the UV–vis spectra from 4.4 to 2.5 eV. Temperature was monitored and controlled through a Keck-Clamp fiber cable routed through the sample probe and mounted adjacent to the sample substrate. A positive and negative field sweep scan from 0 to 6 T was performed for the stannate samples at 40 ± 0.5 K in 2 T intervals. The collected spectra were corrected by subtracting the 0 T scan to reduce artifacts from polarization effects, magnetic field inhomogeneity, and other anomalies during spectral measurements.

Multinuclear Solid-State NMR (SSNMR) Characterization: ^{113}Cd and ^{119}Sn SSNMR experiments were performed using a Bruker NEO console with an Oxford 18.8 T ($v_0(^1\text{H})$ = 800 MHz) magnet operating at $v_0(^{113}\text{Cd})$ = 177.545 MHz and $v_0(^{119}\text{Sn})$ = 298.325 MHz, respectively. A home-built 3.2 mm HXY MAS probe was used for all NMR experiments performed at 18.8 T. Pulse width calibrations and chemical shift reference frequencies for all nuclei were calculated using their respective solid-state standards. ^{113}Cd and ^{119}Sn chemical shifts were reported with respect to Cd(ClO$_4$)$_2$ and Sn(CH$_3$)$_4$ (δ_{iso} = 0 ppm) using Cd(NO$_3$)$_2$•4H$_2$O (δ_{iso} = −102 ppm) and solid SnO (δ_{iso} = 121 ppm), respectively, as secondary references. The experimental conditions and acquisition parameters for each class of experiments, which include basic ^{1}H-X CP/MAS,[112] ^{1}H-X CP/CPMG,[113,114] and direct excitation WURST-CPMG[115] are summarized in Tables S3 and S4 (Supporting Information).

Supporting Information

Supporting Information is available from the Wiley Online Library or from the author.

Conflict of Interest

The authors declare no conflict of interest.

Author Contributions

The manuscript was written through the contributions of all authors. All authors have given approval to the final version of the manuscript. R.E.O performed conceptualization, formal analysis, investigation, methodology, software, validation, and visualization, and wrote, reviewed, and edited the original draft. J.E.K. performed Investigation, methodology, formal analysis, software, investigation, wrote, reviewed, and edited. R.S. performed conceptualization, formal analysis, investigation, methodology, software, and validation, wrote, reviewed, and edited. A.B. performed Investigation, and methodology, wrote, reviewed, and edited. S.A.M. performed methodology, resources, funding acquisition, and supervision, wrote, reviewed, and edited. N.J.H. performed resources, funding, acquisition, and supervision, wrote, reviewed, and edited. G.F.S. performed conceptualization, funding acquisition, methodology, and supervision, and wrote, reviewed, and edited the original draft.

Data Availability Statement

The data that support the findings of this study are available from the corresponding author upon reasonable request.

[1] R. Verma, R. Belgamwar, V. Polshettiwar, *ACS Mater. Lett.* **2021**, *3*, 574.
[2] Y. H. Jang, Y. J. Jang, S. Kim, L. N. Quan, K. Chung, D. H. Kim, *Chem. Rev.* **2016**, *116*, 14982.
[3] A. M. Shrivastav, U. Cvelbar, I. Abdulhalim, *Commun. Biol.* **2021**, *4*, 70.
[4] W. O. F. Carvalho, J. R. Mejía-Salazar, *Sensors* **2020**, *20*, 2488.
[5] N. Cohen, A. Zussman, G. Sarusi, *Infrared Phys. Technol.* **2001**, *42*, 391.
[6] H. Villuendas, C. Vilches, R. Quidant, *ACS Nanosci. Au* **2023**, *3*, 347.
[7] Y. Zhong, Z. Liu, E. Sarnello, T. Li, Y. Liu, J. Chen, X. Ye, *Chem. Mater.* **2021**, *33*, 1954.
[8] T. R. Gordon, T. Paik, D. R. Klein, G. V. Naik, H. Caglayan, A. Boltasseva, C. B. Murray, *Nano Lett.* **2013**, *13*, 2857.
[9] Z. Liu, Y. Zhong, I. Shafei, S. Jeong, L. Wang, H. T. Nguyen, C. J. Sun, T. Li, J. Chen, L. Chen, Y. Losovyj, X. Gao, W. Ma, X. Ye, *Nano Lett.* **2020**, *20*, 2821.
[10] K. Manthiram, A. P. Alivisatos, *J. Am. Chem. Soc.* **2012**, *134*, 3995.
[11] C. R. Conti, J. R. McBride, G. F. Strouse, *J. Phys. Chem. C* **2021**, *125*, 7772.
[12] M. Anitha, K. Saravanakumar, N. Anitha, L. Amalraj, *Opt. Quant. Electron* **2019**, *51*, 187.
[13] B. H. Kim, C. M. Staller, S. H. Cho, S. Heo, C. E. Garrison, J. Kim, D. J. Milliron, *ACS Nano* **2018**, *12*, 3200.
[14] W. Yu, J. G. Lee, Y.-H. Joo, B. Hou, D.-S. Um, C.-I. Kim, *Appl. Phys. A* **2022**, *128*, 942.

**ADVANCED
SCIENCE NEWS**

www.advancedsciencenews.com

**ADVANCED
OPTICAL
MATERIALS**

www.advopticalmat.de

[15] S. N. Vidhya, O. N. Balasundaram, M. Chandramohan, *J. Saudi Chem. Soc.* **2016**, *20*, 703.

[16] J. K. Saha, R. N. Bukke, N. N. Mude, J. Jang, *Sci. Rep.* **2020**, *10*, 8999.

[17] S. D. Ponja, S. Sathasivam, I. P. Parkin, C. J. Carmalt, *Sci. Rep.* **2020**, *10*, 638.

[18] J. Kim, A. Agrawal, F. Krieg, A. Bergerud, D. J. Milliron, *Nano Lett.* **2016**, *16*, 3879.

[19] N. Petrini, M. Ghini, N. Curreli, I. Kriegel, *J. Phys. Chem. C* **2023**, *127*, 1576.

[20] B. J. Roman, S. A. Shubert-Zuleta, G. Shim, V. Kyveryga, M. Faris, D. J. Milliron, *J. Phys. Chem. C* **2023**, *127*, 2456.

[21] C. R. Conti III, G. Quiroz-Delfi, J. S. Schwarck, B. Chen, G. F. Strouse, *J. Phys. Chem. C* **2020**, *124*, 28220.

[22] Z. Liu, R. Beaulac, *Chem. Mater.* **2017**, *29*, 7507.

[23] J. T. Lee, S. Hati, M. M. Fahey, J. M. Zaleski, R. Sardar, *Chem. Mater.* **2022**, *34*, 3053.

[24] J. E. Kuszynski, J. C. Kays, C. R. Conti, S. A. McGill, A. M. Dennis, G. F. Strouse, *J. Phys. Chem. C* **2022**, *126*, 12669.

[25] J. E. Kuszynski, C. J. Fabiano, E. T. Nguyen, K. Mao, A. K. Ahuja, R. D. Schaller, G. F. Strouse, *J. Phys. Chem. C* **2023**, *127*, 22654.

[26] Y. Shi, P. F. Ndione, L. Y. Lim, D. Sokaras, T.-C. Weng, A. R. Nagaraja, A. G. Karydas, J. D. Perkins, T. O. Mason, D. S. Ginley, A. Zunger, M. F. Toney, *Chem. Mater.* **2014**, *26*, 1867.

[27] M. E. Foley, R. W. Meulenberg, J. R. McBride, G. F. Strouse, *Chem. Mater.* **2015**, *27*, 8362.

[28] D. A. Hardy, R. A. Tigaa, J. R. McBride, R. E. Ortega, G. F. Strouse, *J. Am. Chem. Soc.* **2019**, *141*, 20416.

[29] M. N. Da Silva, J. M. De Carvalho, M. C. De Abreu Fantini, L. A. Chiavacci, C. Bourgaux, *ACS Appl. Nano Mater.* **2019**, *2*, 6918.

[30] S. Cho, Y. Kim, A. DiVenere, G. K. Wong, J. B. Ketterson, J. R. Meyer, *Appl. Phys. Lett.* **1999**, *75*, 1401.

[31] W. C. Yang, Y. T. Xie, W. K. Zhu, K. Park, A. P. Chen, Y. Losovyj, Z. Li, H. M. Liu, M. Starr, J. A. Acosta, C. G. Tao, N. Li, Q. X. Jia, J. J. Heremans, S. X. Zhang, *Sci. Rep.* **2017**, *7*, 7740.

[32] S. B. Zhang, S.-H. Wei, *Appl. Phys. Lett.* **2002**, *80*, 1376.

[33] C. Urso, M. Barawi, R. Gaspari, G. Sirigu, I. Kriegel, M. Zavelani-Rossi, F. Scotognella, M. Manca, M. Prato, L. De Trizio, L. Manna, *J. Am. Chem. Soc.* **2017**, *139*, 1198.

[34] S. T. Hartman, G. J. Pilania, *Phys. Chem. Solids* **2022**, *168*, 110822.

[35] Y. Dou, R. G. Egdell, *Phys. Rev. B* **1996**, *53*, 15405.

[36] W. P. Mulligan, T. J. Coutts, *MRS Proc.* **1997**, *471*, 117.

[37] E. Leja, T. Stapiński, K. Marszałek, *Thin Solid Films* **1985**, *125*, 119.

[38] T. J. Coutts, D. L. Young, X. Li, W. P. Mulligan, X. Wu, *J. Vac. Sci. Technol. A* **2000**, *18*, 2646.

[39] G. Haacke, W. E. Mealmaker, L. A. Siegel, *Thin Solid Films* **1978**, *55*, 67.

[40] A. J. Nozik, *Phys. Rev. B* **1972**, *6*, 453.

[41] G. Haacke, *Appl. Phys. Lett.* **1976**, *28*, 622.

[42] L. A. Siegel, *J. Appl. Crystallogr.* **1978**, *11*, 284.

[43] A. M. Schimpf, N. Thakkar, C. E. Gunthardt, D. J. Masiello, D. R. Gamelin, *ACS Nano* **2014**, *8*, 1065.

[44] E. Burstein, *Phys. Rev.* **1954**, *93*, 632.

[45] T. S. Moss, *Proc. Phys. Soc. B* **1954**, *67*, 775.

[46] L. B. Casabianca, *Solid State Nucl. Magn. Reson.* **2020**, *107*, 101664.

[47] L. E. Marbella, J. E. Millstone, *Chem. Mater.* **2015**, *27*, 2721.

[48] W. D. Knight, *Phys. Rev.* **1949**, *76*, 1259.

[49] A. Abragam, *The Principles of Nuclear Magnetism*, Clarendon Press, Oxford **1961**.

[50] C. P. Slichter, *Phil. Mag. B* **1999**, *79*, 1253.

[51] J. J. Van Der Klink, J. Buttet, M. Graetzel, *Phys. Rev. B* **1984**, *29*, 6352.

[52] H. E. Rhodes, P. K. Wang, H. T. Stokes, C. P. Slichter, J. H. Sinfelt, *Phys. Rev. B* **1982**, *26*, 3559.

[53] R. E. Taylor, F. Alkan, D. Koumoulis, M. P. Lake, D. King, C. Dybowski, L.-S. Bouchard, *J. Phys. Chem. C* **2013**, *117*, 8959.

[54] B. N. Ganguly, *Phys. Rev. B* **1973**, *8*, 1055.

[55] J. M. Titman, *Phys. Rep.* **1977**, *33*, 1.

[56] E. M. Levin, B. A. Cook, K. Ahn, M. G. Kanatzidis, K. Schmidt-Rohr, *Phys. Rev. B* **2009**, *80*, 115211.

[57] R. W. Schurko, in *eMagRes*, John Wiley & Sons, Ltd, Hoboken, NJ **2011**.

[58] R. W. Schurko, *Acc. Chem. Res.* **2013**, *46*, 1985.

[59] L. H. Bennett, R. E. Watson, G. C. Carter, *J. Res.* **1970**, *74A*, 569.

[60] R. K. Mishra, G. Thomas, *J. Appl. Phys.* **1977**, *48*, 4576.

[61] T. Meng, B. McCandless, W. Buchanan, E. Kimberly, R. Birkmire, *J. Alloys Compd.* **2013**, *556*, 39.

[62] A. Agrawal, I. Kriegel, D. J. Milliron, *J. Phys. Chem. C* **2015**, *119*, 6227.

[63] D. Y. Kim, W. Li, Y. Ma, T. Yu, Z. Y. Li, O. O. Park, Y. Xia, *Chem. – Eur. J.* **2011**, *17*, 4759.

[64] S. D. Lounis, E. L. Runnerstrom, A. Bergerud, D. Nordlund, D. J. Milliron, *J. Am. Chem. Soc.* **2014**, *136*, 7110.

[65] S. Ghosh, M. Saha, S. Paul, S. K. De, *Small* **2017**, *13*, 1602469.

[66] C. M. Staller, S. L. Gibbs, C. A. Saez Cabezas, D. J. Milliron, *Nano Lett.* **2019**, *19*, 8149.

[67] P. K. Jain, K. S. Lee, I. H. El-Sayed, M. A. El-Sayed, *J. Phys. Chem. B* **2006**, *110*, 7238.

[68] O. Zandi, A. Agrawal, A. B. Shearer, L. C. Reimnitz, C. J. Dahlman, C. M. Staller, D. J. Milliron, *Nat. Mater.* **2018**, *17*, 710.

[69] S. A. Shubert-Zuleta, B. Tandon, B. J. Roman, X. Y. Gan, D. J. Milliron, *Chem. Mater.* **2023**, *35*, 3880.

[70] F. Pineider, G. Campo, V. Bonanni, C. D. J. Fernández, G. Mattei, A. Caneschi, D. Gatteschi, C. Sangregorio, *Nano Lett.* **2013**, *13*, 4785.

[71] K. H. Hartstein, A. M. Schimpf, M. Salvador, D. R. Gamelin, *J. Phys. Chem. Lett.* **2017**, *8*, 1831.

[72] B. Han, X. Gao, J. Lv, Z. Tang, *Adv. Mater.* **2020**, *32*, 1801491.

[73] P. Yin, S. Chen, P. V. Radovanovic, *J. Phys. Chem. Lett.* **2022**, *13*, 5545.

[74] B. Tandon, P. V. Radovanovic, *ACS Nano* **2023**, *17*, 14069.

[75] P. Jayaram, T. P. Jaya, K. Prasanth, A. K. Abdul Gafoor, P. P. Pradyumnan, *Trans. Ind. Inst. Met.* **2011**, *64*, 221.

[76] M. M. El-Nahass, A. A. Atta, M. M. Abd El-Raheem, A. M. Hassanien, *J. Alloys Compd.* **2014**, *585*, 1.

[77] S.-H. Wei, D. Segev, *Phys. Rev. B* **2005**, *71*, 1.

[78] C. J. Barrows, V. A. Vlaskin, D. R. Gamelin, *J. Phys. Chem. Lett.* **2015**, *6*, 3076.

[79] S. Kolahi, S. Farjami-Shayesteh, Y. Azizian-Kalandaragh, *Mater. Sci. Semicond. Process.* **2011**, *14*, 294.

[80] S. L. Gibbs, C. M. Staller, A. Agrawal, R. W. Johns, C. A. S. Cabezas, D. J. Milliron, *J. Phys. Chem. C* **2020**, *124*, 24351.

[81] M. G. Berrettini, G. Braun, J. G. Hu, G. F. Strouse, *J. Am. Chem. Soc.* **2004**, *126*, 7063.

[82] C. Kittel, *Introduction to Solid State Physics*, Wiley, Hoboken, NJ **2005**.

[83] Q. Li, L. Sui, G. Niu, J. Jiang, Y. Zhang, L. Che, G. Wu, K. Yuan, *Phys. Rev. B* **2021**, *103*, 125416.

[84] C. H. Townes, C. Herring, W. D. Knight, *Phys. Rev.* **1950**, *77*, 852.

[85] M. N. Alexander, D. F. Holcomb, *Rev. Mod. Phys.* **1968**, *40*, 815.

[86] L. E. Marbella, X. Y. Gan, D. C. Kaseman, J. E. Millstone, *Nano Lett.* **2017**, *17*, 2414.

[87] S. H. Cho, S. Ghosh, Z. J. Berkson, J. A. Hachtel, J. Shi, X. Zhao, L. C. Reimnitz, C. J. Dahlman, Y. Ho, A. Yang, Y. Liu, J.

C. Idrobo, B. F. Chmelka, D. J. Milliron, *Chem. Mater.* **2019**, *31*, 2661.

[88] C. M. Cardile, R. H. Meinhold, K. J. D. MacKenzie, *J. Phys. Chem. Solids* **1987**, *48*, 881.

[89] R. K. Sundfors, D. F. Holcomb, *Phys. Rev.* **1964**, *136*, A810.

[90] E. M. Meintjes, W. W. Warren, J. P. Yesinowski, *Solid State Nucl. Magn. Reson.* **2013**, *55–56*, 91.

[91] J. Y. Leloup, B. Sapoval, G. Martinez, *Phys. Rev. B* **1973**, *7*, 5276.

[92] K. Lee, J. Liesegang, P. B. P. Phipps, *Phys. Rev.* **1967**, *161*, 322.

[93] D. D. Lovingood, R. Achey, A. K. Paravastu, G. F. Strouse, *J. Am. Chem. Soc.* **2010**, *132*, 3344.

[94] D. D. Lovingood, R. E. Oyler, G. F. Strouse, *J. Am. Chem. Soc.* **2008**, *130*, 17004.

[95] R. S. Honkonen, F. D. Doty, P. D. Ellis, *J. Am. Chem. Soc.* **1983**, *105*, 4163.

[96] C. I. Ratcliffe, K. Yu, J. A. Ripmeester, M. Badruz Zaman, C. Badarau, S. Singh, *Phys. Chem. Chem. Phys.* **2006**, *8*, 3510.

[97] T. M. Duncan, *A Compilation of Chemical Shift Anisotropies*, Farragut Press, Chicago **1990**.

[98] M. Schlaak, A. Weiss, *Solid State Commun.* **1970**, *8*, 1241.

[99] G. J. Rees, S. T. Orr, L. O. Barrett, J. M. Fisher, J. Houghton, G. H. Spikes, B. R. C. Theobald, D. Thompsett, M. E. Smith, J. V. Hanna, *Phys. Chem. Chem. Phys.* **2013**, *15*, 17195.

[100] S. L. Gibbs, C. M. Staller, D. J. Milliron, *Acc. Chem. Res.* **2019**, *52*, 2516.

[101] K. J. D. MacKenzie, M. E. Smith, *Multinuclear Solid-State NMR of Inorganic Materials*, Elsevier, Pergamon, Oxford **2002**.

[102] C. Cossement, J. Darville, J.-M. Gilles, J. B. Nagy, C. Fernandez, J.-P. Amoureux, *Magn. Reson. Chem.* **1992**, *30*, 263.

[103] Y. Shen, A. Roberge, R. Tan, M. Y. Gee, D. C. Gary, Y. Huang, D. A. Blom, B. C. Benicewicz, B. M. Cossairt, A. B. Greytak, *Chem. Sci.* **2016**, *7*, 5671.

[104] A. Chatzigoulas, K. Karathanou, D. Dellis, Z. Cournia, *J. Chem. Inf. Model.* **2018**, *58*, 2380.

[105] K. F. Garrity, J. W. Bennett, K. M. Rabe, D. Vanderbilt, *Comput. Mater. Sci.* **2014**, *81*, 446.

[106] G. Prandini, A. Marrazzo, I. E. Castelli, N. Mounet, N. Marzari, *npj Comput. Mater.* **2018**, *4*, 72.

[107] P. Giannozzi, S. Baroni, N. Bonini, M. Calandra, R. Car, C. Cavazzoni, D. Ceresoli, G. L. Chiarotti, M. Cococcioni, I. Dabo, A. Dal Corso, S. de Gironcoli, S. Fabris, G. Fratesi, R. Gebauer, U. Gerstmann, C. Gougoussis, A. Kokalj, M. Lazzeri, L. Martin-Samos, N. Marzari, F. Mauri, R. Mazzarello, S. Paolini, A. Pasquarello, L. Paulatto, C. Sbraccia, S. Scandolo, G. Sclauzero, A. P. Seitsonen, et al., *J. Phys.: Condens. Matter* **2009**, *21*, 395502.

[108] M. E. Bowden, C. M. Cardile, *Powder Diffr.* **1990**, *5*, 36.

[109] Y. Hinuma, G. Pizzi, Y. Kumagai, F. Oba, I. Tanaka, *Comput. Mater. Sci.* **2017**, *128*, 140.

[110] H. J. Monkhorst, J. D. Pack, *Phys. Rev. B* **1976**, *13*, 5188.

[111] M. Tang, J. Shang, Y. Zhang, *Chinese Phys. B* **2018**, *27*, 017101.

[112] A. Pines, M. G. Gibby, J. S. Waugh, *J. Chem. Phys.* **2003**, *59*, 569.

[113] R. Siegel, T. T. Nakashima, R. E. Wasylishen, *Concepts Magn. Reson. Part A* **2005**, *26A*, 62.

[114] I. Hung, A. J. Rossini, R. W. Schurko, *J. Phys. Chem. A* **2004**, *108*, 7112.

[115] L. A. O'Dell, R. W. Schurko, *Chem. Phys. Lett.* **2008**, *464*, 97.